ARTICLE

Check for updates

High-harmonic generation in CdTe with ultra-low pump intensity and high photon flux

Zhe Long[1,5], Hang Yang[1,5], Kan Tian[1], Linzhen He[1], Rui Qin[2], Zi-Yu Chen [3✉], Qi Jie Wang [4] & Houkun Liang [1✉]

An ultra-low pump intensity and high photon flux have been long pursuits of high harmonic generation (HHG) in solids. However, there is lack of a criterion to identify a pristine solid material exhibiting such characteristics. Here, we report systematic investigation into HHG from a cadmium telluride (CdTe) bulk crystal with a flat band dispersion near the Fermi level which leads to a large density of states. The measured pump intensity for the 31st harmonics (229 nm) is only 75 GW/cm^2, one order of magnitude lower than that of other pristine crystals including two-dimensional materials reported so far. A comparative measurement shows CdTe has two-to-three orders of magnitude stronger HHG than silicon does, and high HHG yields in the ultraviolet region compared to GaSe. A high photon flux of ~ 6 × 10^{12} photons/s (5th−8th) with a robust long-time sustainability is obtained. This work offers a route towards compact vacuum ultraviolet laser sources.

[1] School of Electronics and Information Engineering, Sichuan University, Chengdu, Sichuan 610064, China. [2] National Key Laboratory of Shock Wave and Detonation Physics, Institute of Fluid Physics, China Academy of Engineering Physics, Mianyang 621999, China. [3] Key Laboratory of High Energy Density Physics and Technology (MoE), College of Physics, Sichuan University, Chengdu 610064, China. [4] School of Electrical & Electronic Engineering & The Photonics Institute, Nanyang Technological University, 639798 Singapore, Singapore. [5]These authors contributed equally: Zhe Long, Hang Yang. ✉email: ziyuch@scu.edu.cn; hkliang@scu.edu.cn

High harmonic generation (HHG), traditionally occurred in rare-gas atoms irradiated by intense laser pulses, has been extensively explored as coherent light sources with short wavelength in the vacuum-extreme ultraviolet spectral region and ultrashort duration in the attosecond regime. In recent years, HHG in solids has been observed from a wide variety of materials and attracted a great deal of attention. Typical examples include dielectrics such as ZnO[1], MgO[2], silicon[3], SiO_2[4], sapphire[5], and GaSe[6,7] as well as two-dimensional materials like MoS_2[8], graphene[9]. In Table 1, we present a survey of representative works of HHG in solids with five categories of materials as bulk, thin films, two-dimensional materials, topologically protected materials, and materials with meta-structures, where the experimentally reported key parameters of HHG such as the pump wavelength, the maximal pump intensity, and the highest harmonic energy and order, as well as the corresponding pump intensity, are summarized. Compared to its gas-phase counterpart, HHG in the condensed phase allows more compact coherent ultrafast photonic devices with lower driving laser intensities. The typical laser intensity to drive this extreme nonlinear optical process in solids including bulk and two-dimensional materials is as low as $10^{11}-10^{12}$ W/cm^2, which is two or three orders of magnitude lower than that in gases. To further lower the pump intensity, near-field enhancement methods based on plasmonic resonances employing metallic or dielectric nanostructures deposited on solid surfaces have been demonstrated[10–14]. The driving laser intensity at the level of 10^{10} W/cm^2 can be achieved. However, apart from manufacturing difficulties, the nanostructures suffer from shortcomings of low damage intensity and small enhancement areas. Moreover, the resonance-based methods can only enhance laser fields with a particular wavelength, determined by the materials and their structural designs. To increase the enhancement volume, epsilon-near-zero materials such as indium-doped CdO thin film have been adopted[15]. The pump intensity can be further reduced by one order of magnitude, however, the laser wavelength that can be enhanced is also fixed by the doping level of the material. In addition, the damage threshold of the doped thin film is usually small. Therefore, it is desirable to discover a pristine and versatile solid material

exhibiting low pump intensity even without field enhancement and high damage threshold.

As the microscopic mechanisms of HHG in solids, both interband (induced by polarization between conduction and valence bands) and intraband (originated from non-parabolic band dispersion) contributions, are closely associated with the electronic structure of the material, a possible approach towards searching for ideal material candidates is to generally examine the band structure at first. Previous theoretical studies have predicted phosphorene (a monolayer black phosphorus) displaying good HHG properties which can be attributed to its unique band structure[16]. An impressive feature of the band structure of phosphorene is a relatively flat dispersion of the valence band near the Fermi level, which leads to a large density of states (DOS) and thus substantial excitation of electrons. Aside from that, phosphorene has a moderate and direct band gap of ~2.0 eV[17] and high free-carrier mobility of ~1000 cm^2/V/s[18]. These theoretical studies shed light on the signatures of materials suitable for HHG, although HHG in phosphorene is difficult to realize experimentally due to the fabrication requirement and unstable characteristics of phosphorene. Fortunately, there do exist materials not only exhibiting similar electronic properties to that of phosphorene (i.e., flat shape of band dispersion near the Fermi level, moderate direct band gap, and high carrier mobility), but also being chemically stable and robust, as well as easy to obtain.

Here we report on systematic experimental investigation to demonstrate cadmium telluride (CdTe) being one of such excellent candidates. The electronic structures and ultrafast carrier dynamics of CdTe enable ultra-low pump intensity and high-efficiency harmonics emission. In experiment, the measured pump intensity for the 12th and 31st harmonic order is only 30 and 75 GW/cm^2, respectively, which is similar to or even smaller than that of the dielectrics with plasmonic meta-structures for the HHG enhancement. The HHG output grows with the pump intensity up to 4.5 TW/cm^2 without saturation. A comparative measurement shows CdTe has two-to-three orders of magnitude stronger HHG than that of silicon, and high HHG yields in the ultraviolet region compared to common HHG dielectric such as

---

Table 1 Comparison of HHG in CdTe (yellow) with other commonly used materials of HHG in solids.

Materials	Pump wavelength (μm)	The maximal pump intensity (TW/cm^2)	The highest harmonic energy (eV) and order (the corresponding pump intensity (TW/cm^2))	Reference
Si	3.5		6, 17th (0.26)	3
Sapphire	0.8	1.31	20.2, 13th (1.1)	5
ZnO	3.25	5	9.5, 25th (5)	1
GaSe	10	13.7	2.7, 22nd (13.7)	7
Graphene	4.77	1.7	2.3, 9th (1.7)	9
MoS_2	4.13	2.2	3.9, 13th (1.8)	8
β-WP$_2$	1.9	1.2	6.5, 10th (0.23)	42
ZnO nanostructure	2–2.3	1	5.4, 9th (1)	14
GaP metamaterial	3.7−4	0.6	2.8, 9th (0.062)	11
Si metamaterial	2.2−2.3	0.3	4.8, 9th (0.2)	10
Si plasmonics	2.1	0.2	5.3, 9th (0.02)	13
Sapphire metamaterial	0.8	0.42	20.2, 13th (0.1)	12
Perovskite thin film	3.5	0.45	4.6, 13th (0.45)	25
Si-sapphire interface	2.2	5.6	7.3, 13th (3.2)	43
WSe_2 nanosheet	0.764	0.767	35.6, 22nd (0.767)	26
CdO	2.08	0.014	5, 9th (0.014)	14
Bi_2Se_3	5	0.054	2.7, 11th (0.054)	27
1 T′ MoSSe	5	1.06	4.96, 20th (1.06)	28
CdTe	7.1	4.5	5.4, 31st (0.075)	This work

The HHG materials are categorized into bulk (green), two-dimensional materials (blue), materials with meta-structures (pink), thin films (grey), and topologically protected materials (orange).
Parameters of the pump wavelength, the maximal pump intensity, and the highest harmonic energy, as well as the corresponding pump intensity, are summarized.
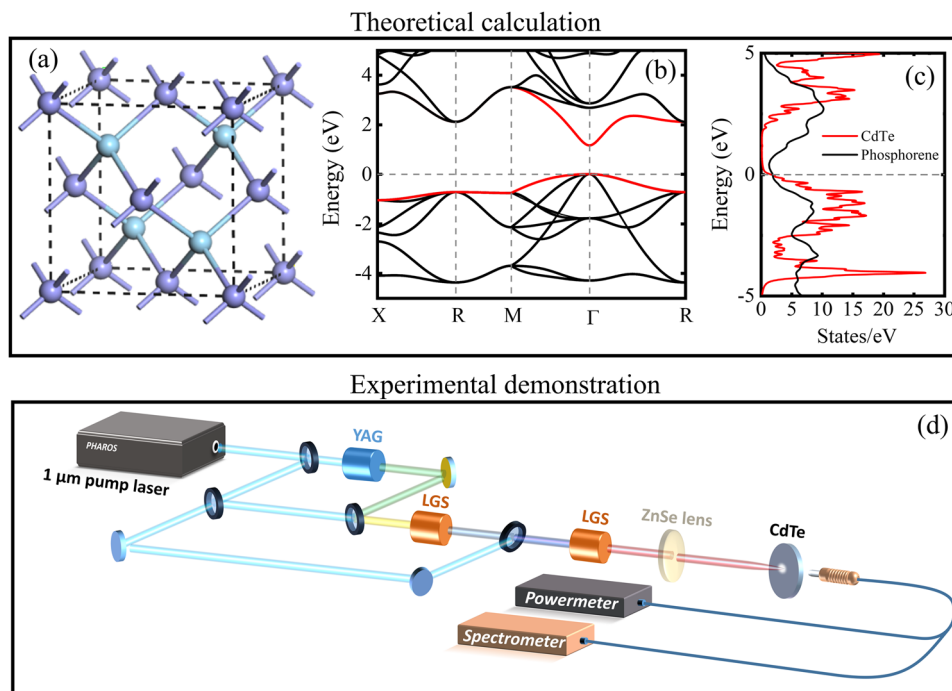
Fig. 1 Theoretical calculation and experimental demonstration of high harmonic generation (HHG) in CdTe. a Crystal structure of the bulk CdTe (111). The balls with different colors represent either the Cd or the Te atoms. **b** The calculated electronic band structure of CdTe. The red curves are the valence band maximum and the conduction band minimum. The flat shape of band dispersion is revealed. At the Γ-point, a moderate direct band gap of ~1.2 eV is obtained. This is lower than the experimental value of 1.44 eV, because, in the DFT calculations, we employ the local density approximation (LDA) for the exchange and correlation functional and do not consider spin-orbit coupling (SOC). However, as demonstrated by previous results, the underestimated bandgap[16] and neglected SOC[41] do not affect the HHG spectra significantly. **c** The comparison of the calculated density of states (DOS) of the single crystal CdTe (red) and phosphorene (black) obtained by first-principles DFT calculations. The gray dashed lines indicate the Fermi level. It is noted that the DOS of CdTe is several times larger at an energy level slightly below the Fermi level. More calculation details are shown in Supplementary Fig. 1. **d** The experimental schematic of HHG in CdTe pumped by mid-infrared femtosecond pulses. The mid-infrared laser is focused by a zinc selenide (ZnSe) lens. The HHG spectra spanning the mid-infrared, near-infrared, visible, and ultraviolet regions are measured by several spectrometers. The output power of the 5th to 8th harmonics is characterized by coupling the emission into a powermeter (JoinwiT, JW2323C). YAG, yttrium aluminum garnet; LGS, LiGaS2 crystal.

GaSe. A high photon flux of ~ 6×10^{12} photons/s (5th−8th) with robust long-time sustainability is also demonstrated.

Results and discussion

First-principles calculations on electronic structures and HHG characteristics. CdTe is a prototypical group II-VI crystalline compound semiconducting material commonly used in the photovoltaic[19] and X-ray detector industry[20]. CdTe crystal has a cubic zinc blende structure, the same as that of the tetrahedral bonding configuration of diamond with each Cd (Te) surrounded by four Te (Cd) atoms (Fig. 1a). The atomic structure thus lacks of spatial inversion symmetry. Although well known as a versatile photon detector for X-ray and widely used in the solar cell thin film photovoltaic technology, the strong-field nonlinear optical properties and ultrafast carrier dynamics of CdTe have never being explored.

Before presenting the experiment data, we first examine the favorable electronic structure of CdTe and its implication for excellent HHG properties using first-principles calculations. Fig. 1b, c shows the band structure and DOS calculated by density functional theory (DFT), respectively. Around the top of the valence band maximum, a relatively flat shape of band dispersion can be clearly seen. This band structure results in a large DOS around the Fermi level. Fig. 1c compares the DOS per atom of CdTe and phosphorene. The DOS of CdTe is larger than that of phosphorene in the valence bands near the Fermi level, albeit large peaks of DOS are located at higher energy levels above the Fermi level in the conduction bands. Besides, CdTe also

possesses a high carrier mobility of ~1100 $cm^2/(V\,s)$[21], close to that of phosphorene. These electronic properties are beneficial for HHG. It has been theoretically demonstrated that phosphorene exhibits good HHG[16], with harmonic intensity one-to-two orders of magnitude higher than that in other typical materials. The similar electronic properties between CdTe and phosphorene suggest that CdTe is also potentially efficient in HHG with more calculation details shown in Supplementary Fig. 1 (see Supplementary Note 1). These first-principles calculation results, in accordance with our aforementioned hint in search of potential material candidates, serve as a rough guide for experimental investigation. With the prediction of promising HHG in CdTe, we show our experimental HHG characterizations in the CdTe bulk crystal.

Ultra-low pump intensity of HHG in the pristine crystal. The CdTe crystal is excited by a mid-infrared (MIR) femtosecond laser centered at 7.1 μm wavelength with a 180 fs pulse width at 50 kHz repetition rate. The experimental schematics are shown in Fig. 1d, with more details shown in ref. [22] and Methods. The excitation photon energy is well below the bandgap of 1.44 eV[23] so the multi-photon ionization is negligible. Fig. 2a shows the transmitted high-order harmonic spectrum generated from the 1-mm-thick CdTe crystal at a pump intensity of 75 GW/cm². Both odd and even harmonics are generated. The highest harmonic reaches the 31st order, corresponding to a wavelength of 229 nm, as shown in the zoom-in Fig. 2b. There are 2 plateaus ranging from the 9th to 14th and 18th to 22nd harmonics, respectively,
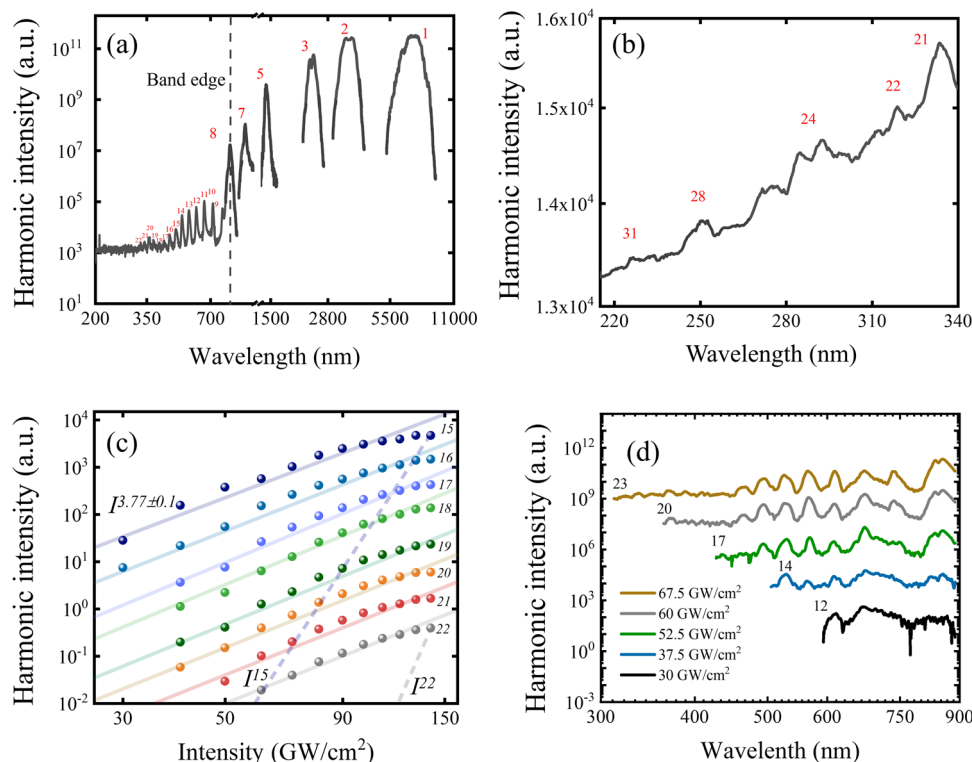
Fig. 2 Measured high harmonic generation (HHG) spectra, strengths and cutoff of different harmonic orders from a CdTe (111) crystal with different pump intensities. a The transmitted HHG spectrum from a 1-mm-thick CdTe (111) at a pump intensity of 75 GW/cm². The vertical dashed line indicates the band edge of the crystal. **b** The zoomed-in HHG spectrum is marked by the dashed square in **a** in the deep ultraviolet region. **c** The individual harmonics strength from 15th to 22nd orders versus the pump intensity. The experimental data is fit based on the power law I^n, for each harmonic as solid lines, where I indicates the pump intensity. The values of n are ~3.8 which is very different from the cases of perturbative nonlinear optics as plotted by the dashed lines. **d** The spectra with the harmonic cutoff ranging from 12th to 23rd orders pumped at an intensity of 30–68 GW/cm². This is 1 order lower than other pristine crystals including two-dimensional materials reported so far, to the best of our knowledge.

which may be associated with the band structure of CdTe. It is worth noting that the harmonics higher than the 9th order are above the bandgap of CdTe, and the harmonics ranging from the 9th to 31st orders are emitted from the last few nanometers of material. The individual harmonics strength of 15th−22nd orders as a function of the pump intensity from 30 to 140 GW/cm² are plotted on a logarithmic scale in Fig. 2c. All harmonic orders match the exponents of a power-law fit of ~3.8, which clearly demonstrates the non-perturbative character of the HHG processes in CdTe even at an intensity level of $10^{10}-10^{11}$ W/cm².

The required minimum pump intensity of HHG in CdTe at which the detector responds is characterized as an important parameter. As shown in Fig. 2d, with a pump intensity of 30 GW/cm², the 12th-order harmonic is generated. The required minimum pump intensity of HHG in CdTe is one order of magnitude lower than that of other bulk crystals[2,3,5,7,24] and two-dimensional materials[8,9]. The required minimum pump intensity of HHG in CdTe is comparable to or even smaller than that of the dielectrics with the aid of plasmonic meta-structures for the HHG enhancement[11–14], the nano-films such as perovskite layer[25] and WSe₂ nanosheet[26], and materials with topologically protected surface states[27,28]. The high-harmonic spectra with harmonic order up to 17, 20, and 23 are measured at a pump intensity of 53, 60, and 68 GW/cm², respectively, with flat spectra over the entire visible spectral range.

To make a direct comparison, the HHG measurements are conducted for two other semiconducting materials, GaSe and Si, the three samples are the same thickness of 1 mm, under the same pump intensity of 80 GW/cm². It is clearly seen from Fig. 3a that no detectable HHG signal is generated from Si. Compared to

GaSe, the above-bandgap harmonics extend to an order of 31st in CdTe, while stop at the 11th order in GaSe corresponding to its bandgap energy. This indicates a much stronger HHG emission in the ultraviolet region from CdTe than GaSe, and verifies a superior character of HHG in CdTe compared to the common dielectrics for harmonics generation.

The HHG cutoff scales linearly with the pump intensities as shown in Fig. 3b, and the 31st-order harmonic is observed at a low pump intensity of only 75 GW/cm². With the flat harmonics spectra and the linear shape of the HHG cutoff with respect to the pump intensity, we suppose HHG emission extending to 100 nm is possible excited by optimized pump wavelength and equipped with vacuum ultraviolet spectrometer and vacuum measurement apparatus. To directly see the advantages of CdTe in reducing the HHG pump intensity, we measure the HHG from silicon and GaSe crystals, common materials for HHG with low pump intensity, under the same experimental conditions as a comparison. It is worth noting that a pump intensity of 180 GW/cm² for silicon is required to generate the 14th harmonic, which is 6-time larger than that of CdTe. For GaSe, a pump intensity of 80 GW/cm² for GaSe is required to generate the 10th harmonic, which is 2.7-time larger than that of CdTe.

High photon flux and damage threshold. The output power of the 5th to 8th harmonics is measured with the pump intensity varying in the range of 0.5 to 4.5 TW/cm², as shown in Fig. 4a. The HHG output grows exponentially with a power-law fit of 1.6−2.6 over the full range of the pump intensity. 4.9 μw harmonics are obtained at a pump power of 210 mW, corresponding
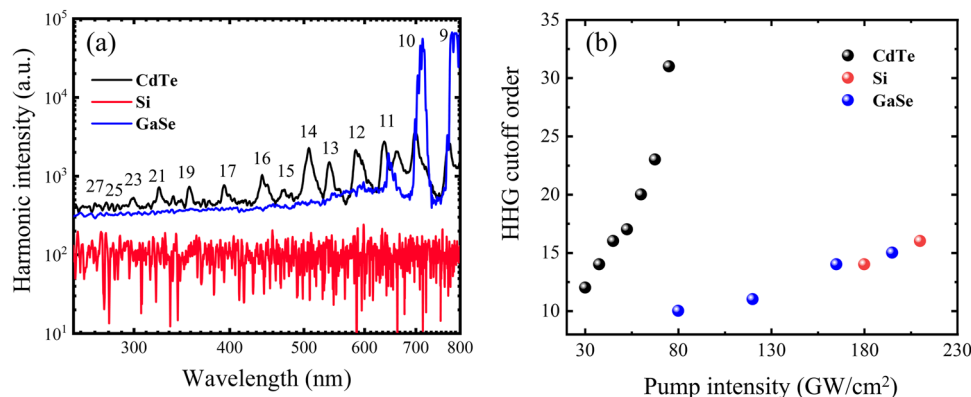
Fig. 3 Comparisons of high harmonic generation (HHG) spectra and cutoffs from CdTe with representative dielectric materials. a The measured transmitted HHG spectra in CdTe (black), GaSe (blue), and Si (red), with the same thickness of 1 mm, under the same pump intensity of 80 GW/cm². **b** The harmonics cutoffs from CdTe (black), Si (red), and GaSe (blue) as the function of pump intensity as denoted by the black, red, and blue symbols, respectively. Much higher pump intensity is required in Si and GaSe to achieve similar cutoffs compared to CdTe.

to a power efficiency of $\sim 2.3 \times 10^{-5}$, which shows the excellent conversion efficiency of CdTe crystal. The harmonics output is reversible and almost returns to the previous values when the pump intensity is decreased, which indicates that there is nearly no obvious damage caused by the strong pump within a short period of exposure time. Although a drop of a few tenths of a microwatt can be seen as the pump intensity is decreased, the overall recurrence trend remains the same. We therefore understand that CdTe not only has a low HHG pump intensity, it can also withstand strong pump intensity which is around one order of magnitude higher than that of the meta-structures and nano-films. The long-term stability of the photon flux from the 5th to 8th order harmonics which is below the bandgap is measured at pump intensities of 0.5 and 2 TW/cm², as shown in Fig. 4b. Photon flux of 1.6×10^{13} photons/s is generated at the first few minutes of excitation, gradually reduced and stabilized to 6×10^{12} photons/s after 20 min of exposure at a pump intensity of 2 TW/cm². The decline of the harmonics photon flux is due to the slow damage of the sample. The result shows that this material can be used for HHG for 30 mins in ambient conditions.

To get a more intuitive sense of the large HHG output from CdTe, we compare its HHG strength with that of silicon under the same experimental conditions. To avoid the measurement error generated from the disturbance of the fluorescence, the HHG strength of CdTe and silicon with photon energy above the bandgap are compared, which means the emission from the last few nanometers of materials is considered. At a pump intensity of 1.1 TW/cm², 9th and 11th harmonics from silicon are barely visible. In sharp contrast, the HHG emission from CdTe saturates the spectrometer. Hence, we have to reduce the pump intensity to 0.2 TW/cm² to fit the HHG emission from CdTe within the dynamic range of the spectrometer. As shown in Fig. 4c, the high harmonic spectra from CdTe are still about two orders of magnitude stronger than that of silicon even with 5 times weaker pump intensity. High HHG yields from CdTe are confirmed by changing the pump wavelength to 3 μm. As shown in Fig. 4d, with a pump intensity of 0.2 TW/cm² at 3 μm, the high harmonic signal from CdTe is two-to-three orders of magnitude stronger than that of silicon, which is consistent with the measurement pumped at 7.1 μm. The photos of much brighter visible light emission from CdTe compared to that of silicon pumped at both 7.1 μm and 3 μm in the ambient light environment are captured and shown in Supplementary Fig. 3 (see Supplementary Note 3), verifying the superior HHG output generated in CdTe.

To test the feasibility of further extending the HHG cutoff, HHG in CdTe driven at 7.1 μm and 3 μm is compared. As shown in

Fig. 4e, the harmonics spectrum pumped at 3 μm is 2–3 orders of magnitude stronger than that driven at 7 μm, and the spectrum in the deep ultraviolet (DUV) band is relatively flat, pumped at 3 μm. In addition, the cutoff energy is extended from 4.9 to 5.6 eV by changing the pump wavelength from 7.1 to 3 μm. The clear strong 14th harmonics at the wavelength of 220 nm (5.6 eV) is measured as shown in the zoom-in HHG spectrum pumped at 3 μm in Fig. 4f, but higher-order harmonics move beyond the response range of the detector. The lack of vacuum ultraviolet (VUV) spectral measurement apparatus limits the measurement of higher cutoff energies, however, based on the high output strength and flat harmonics spectrum in the DUV region, pumped at 3 μm, we foresee that HHG emission extending to VUV (100−200 nm) region is feasible by exciting with an optimized pump wavelength.

Dependence of HHG on crystallographic orientation. To investigate the dependence of HHG in CdTe on crystallographic orientation, the high-harmonic strengths of 9th−22nd orders with different angle θ between the pump polarization (solid pink arrow) and the crystal mirror plane (dashed grey arrow) are measured as shown in Fig. 5a. It is observed that both odd and even harmonics are modulated uniformly by every 60° with near unity modulation depth, as presented in Fig. 5b, which reveals the 6-fold symmetry of CdTe. The intensity is strongest when the pump field is along the CdTe bond direction, i.e., parallel to the mirror plane. In addition, the polarization angle φ of the high harmonic emission from 10th to 14th orders is measured when the pump polarization is along the specific crystal directions $\theta = 0°$ and $\theta = 30°$, respectively. As shown in Fig. 5c, d, it is observed that the odd harmonics keep along with the pump polarization at both $\theta = 0°$ and $\theta = 30°$, whereas the polarization direction of even orders switches from parallel to perpendicular with respect to the pump when the pump polarization changes from $\theta = 0°$ to $\theta = 30°$. This response is similar to the results observed by the previous works in MoS$_2$[8] and GaSe[24] and in accordance with symmetry requirements of the crystals with broken inversion symmetry. When the pump field is parallel to the mirror plane ($\theta = 0°$), no harmonic is allowed in the direction perpendicular to the pump field because the mirror symmetry is not broken in this direction. While the pump field is perpendicular to the mirror plane ($\theta = 30°$), however, the even orders parallel to the pump field must vanish because the required even harmonic optical responses perpendicular to the mirror plane cancel each other as they exhibit equal amplitude but opposite sign, separated by half laser period due to the combined mirror symmetry of crystal and laser field. In this case, even harmonics
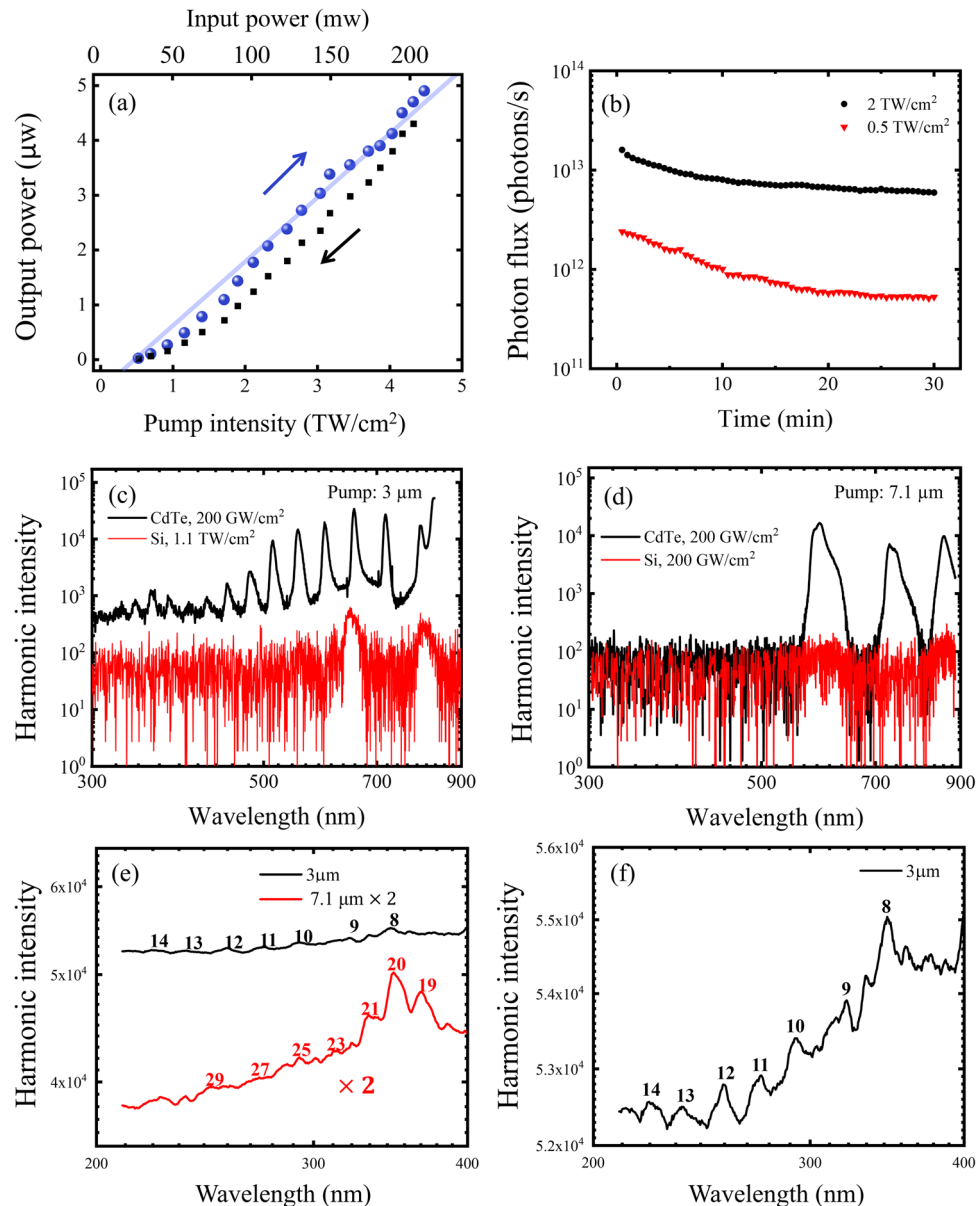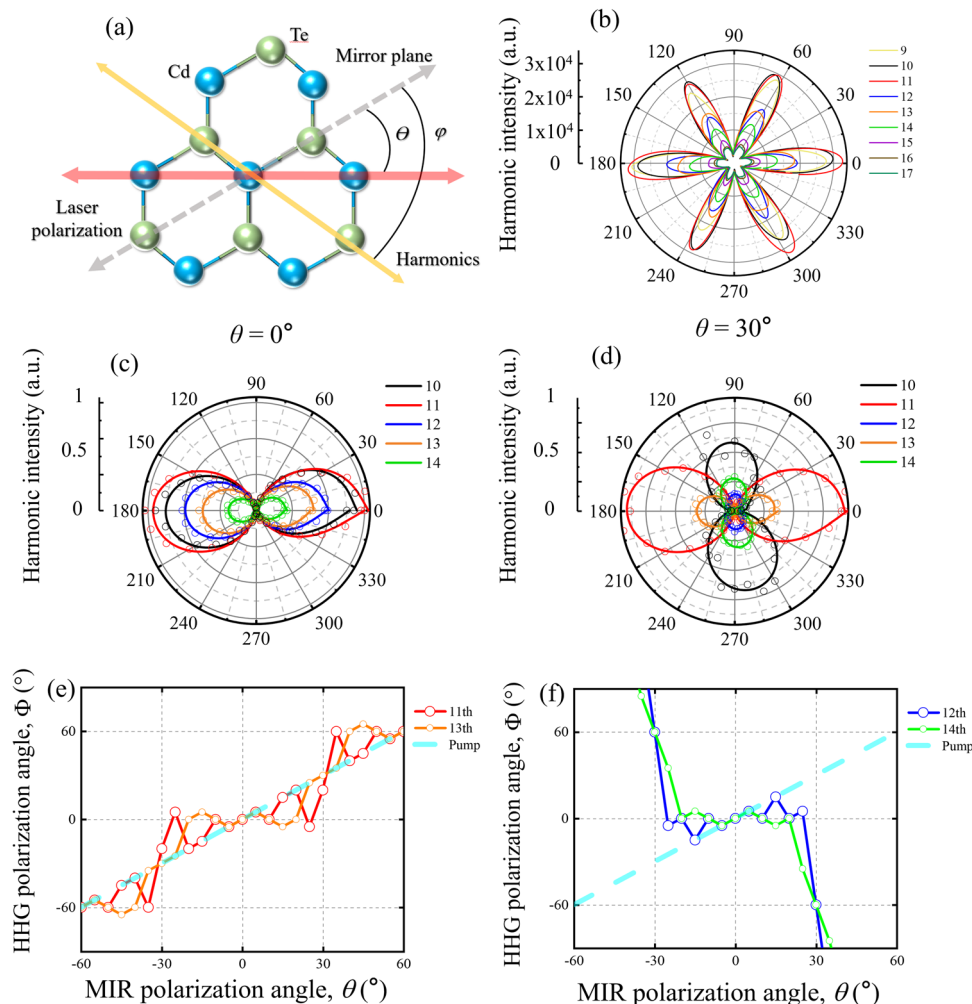
Fig. 4 Measured high harmonic generation (HHG) output power and photon flux in CdTe, and the comparison of the HHG emission between CdTe and silicon pumped at different wavelengths. a The output power of the 5th to 8th harmonics as a function of pump intensities. The blue and black symbols denote the recorded output power when the pump intensity is gradually increased and then reduced, respectively. The harmonics output almost returns to the previous values when the pump intensity is decreased, which implies that there is almost no damage within a short period of exposure time. **b** The long-term stability measurement of the photon flux from 5th to 8th harmonics at 0.5 (red triangles) and 2 (black circles) TW/cm^2 pump intensities. Photon flux of 1.6×10^{13} photons/s is generated at the first few minutes of excitation, gradually reduced, and stabilized to 6×10^{12} photons/s after 20 min of exposure. The decline of the harmonics photon flux is due to the slow damage of the sample. **c** The measured HHG spectra from CdTe (black) and silicon (red) under 0.2 TW/cm^2 and 1.1 TW/cm^2 pump at 7.1 μm, respectively. **d** The HHG spectra under 3 μm pump from CdTe (black) and silicon (red) with the same intensity of 0.2 TW/cm^2. The HHG in CdTe from the measured spectra is 2-to-3 orders stronger than that in silicon. **e** The measured HHG spectra from CdTe under 600 GW/cm^2 pumped at 7.1 (red) and 3 μm (black), respectively. The HHG intensity driven at 7 μm is multiplied by 2. **f** The zoomed-in HHG spectrum pumped at 3 μm in **e**.

can still appear in the direction perpendicular to the pump field, the origin of which may be explained by a Berry curvature term in the intraband semiclassical model as shown in ref. [8]. Berry curvature can act like an out-of-plane magnetic field that gives rise to an anomalous in-plane current perpendicular to the pump field. Fig. [5]d also shows the even harmonics are comparable to the neighboring odd harmonics, indicating the possibly large effect of Berry curvature and non-perturbative nature of the HHG process. This also shows HHG in CdTe may have important contributions from intraband dynamics.

In addition to analyzing harmonic polarization for specific crystal orientation, we also investigate harmonic polarization for different MIR polarization angles to gain further insight into the HHG mechanisms. The polarization angle φ of the high harmonic emission in CdTe is measured, when the pump polarization θ is rotated, as described in[29]. As shown in Fig. 5e, polarizations of even order harmonics (12th and 14th order) are fixed along the crystal mirror planes for the parallel excitation ($\theta \approx 0°$), similar to the behavior of even order harmonics from transition-metal dichalcogenides (TMDCs) in ref. [29] which is

Fig. 5 High-harmonics strength from a CdTe crystal as a function of the pump polarization angle θ and the high harmonic generation (HHG) polarization angle φ. a Schematic diagram of the HHG polarization measurement. The pink arrow represents the pump laser polarization, the dashed grey line indicates the symmetry plane of the crystal, θ is the angle between the pump polarization and the symmetry plane of the crystal, and φ is the harmonics polarization angle. The polarization angle φ is measured with a polarizer. **b** The polar plot of the high harmonic strength with respect to the pump laser polarization. The excitation strength is fixed at around 0.55 TW/cm². Both even and odd orders are observed to be modulated with a period of 60°, which reveals the sixfold symmetry of CdTe. The intensity is strongest when the pump field is along the CdTe bond direction, i.e., parallel to the mirror plane. **c** Intensities of the representative 10th to 14th order harmonics in different polarization angle φ for crystal direction θ = 0°. φ = 0 and 180° means harmonic components parallel to the pump polarization. Both the even and odd orders reach their intensity peaks when the harmonic components polarized parallel to the pump. **d** The same as **c**, except for θ = 30°. The intensity peaks of even orders (10th, 12th, 14th) rotate by 90° (the perpendicular components) with respect to **c**. This is attributed to the break of inversion symmetry and Berry curvature term in an intraband semiclassical model. **e** Odd (11th and 13th in red and orange, respectively) and **f**, even (12th and 14th in blue and green, respectively) order harmonics polarization angle φ resolved as a function of the MIR pump (in cyan) polarization angle θ.

attributed to intraband mechanism. While for the odd-order harmonics (11th and 13th order), as shown in Fig. 5f, the harmonics polarization exhibits noticeable modulation around the driving laser polarization, similar to the characteristics of odd-order harmonics from TMDCs in ref. [29] which originates from interband contribution. The distinctly different behaviors of HHG polarization angel as a function of MIR polarization angle for different harmonic orders suggest that the even and odd-order harmonics in CdTe may be attributed to different HHG mechanisms.

Conclusions
In conclusion, we experimentally demonstrate an ultra-low pump intensity and high throughput of HHG emission from the CdTe crystal. The harmonics flux of 6×10^{12} to 1.6×10^{13} photons/s (5th−8th) is obtained, which is sustained for >30 min of

exposure. Therefore, a pulse energy of hundreds of nano-joule which could be provided by more compact and cheaper laser apparatus such as Cr:ZnS oscillator and amplifier[30] or a single-stage MIR optical parametric amplifier (OPA) is able to excite decent harmonics flux. At meanwhile, thanks to the high damage threshold and centimeter-size crystal aperture, high-harmonics energy could be pursued pumped by the advanced MIR optical parametric chirped-pulse amplifiers with multi-milli-joule pulse energy[31–34]. Moreover, HHG from CdTe in VUV region could be explored in the near future.

In addition, beyond light source, HHG in solids serves as a unique tool to investigate light-induced nonequilibrium phases in materials[35,36]. Studying light-induced nonequilibrium phases and ultrafast carrier dynamics in CdTe have important applications, such as the development of infrared and gamma photon detectors, and solar cell thin film photovoltaic technology as well,

where CdTe is an important material that has been widely used. Moreover, high-quality CdTe epi-layers could be grown by mature semiconductor deposition technologies, such as magnetron sputtering. Thus, we look forward to HHG and attosecond devices fabricated based on CdTe thin films. CdTe thin films with nanostructures could also be employed to further enhance the HHG yield.

Thirdly, the fine HHG property of CdTe induced by its flat shape of band dispersion near the Fermi level, the large DOS, and the high carrier mobility provides a possible criterion in searching for suitable HHG materials, which would definitely trigger more research. In future, materials with similar band dispersion and large band gaps could be investigated to improve the output yields of harmonics above the bandgap, which would benefit applications such as optical coherence tomography in the DUV-VUV region[37], UV multispectral imaging[38], investigations of sub-cycle quasi-particle collision[26], Valence electron high precision imaging[39], and ultrafast electron scattering[40].

Methods

Ab-initio TDDFT simulations of HHG in CdTe. The geometric structure relaxation and ground state electronic structure calculation of the CdTe crystal are performed by solving the Kohn–Sham equation using the CASTEP package within the DFT framework with the local density approximation (LDA) for the exchange–correlation function. A plane wave basis set and ultrasoft pseudopotentials are employed. The plane wave cutoff energy is set to be 330 eV. A $7 \times 7 \times 7$ Monkhorst–Pack k-point mesh for Brillouin zone sampling is used for the conventional cell of CdTe, which contains eight atoms. The atomic positions are relaxed until the maximum force on each atom is less than 0.01 eV/A. The optimized lattice constant along each direction is 6.417 Å, which is in agreement with the reported DFT calculation results. Although it is known that LDA functional gives underestimated band gap, it has been demonstrated that it will not considerably affect the HHG spectra[16]. The atomic coordinates of the computational models could be found in Supplementary dataset 1.

The time evolution of electron wave functions and time-dependent electronic current is then investigated by propagating the time-dependent Kohn–Sham equations in real time and real space using the OCTOPUS package within the framework of TDDFT with the adiabatic LDA functional. The grid spacing of the real-space box is 0.4 Bohr, and the time step for time propagation is 6.05 attosecond. A $20 \times 20 \times 20$ Monkhorst–Pack k-point mesh is used for Brillouin zone sampling of the conventional cell. The fully relativistic Hartwigsen, Goedecker, and Hutter pseudopotential is adopted in the calculations.

We consider the driving laser field in the velocity gauge with a wavelength of 1600 nm (corresponding to a photon energy of 0.77 eV). The peak laser intensity is 2×10^{11} W/cm². The laser electric field is linearly polarized in the (111) cutting plane of CdTe crystal. The laser pulse has a sine-square envelope $f(t) = \sin^2(\pi t/2\tau)$ with $\tau = 20$ fs. The carrier-envelop phase is set to be zero, which has been shown to have no influence on the calculation results. Consideration for the parameters of laser wavelength and pulse duration are mainly for the sake of computational efficiency. After obtaining the total time-dependent electronic current $\mathbf{j}(\mathbf{r}, t)$ from the time-evolved wavefunctions, the HHG spectrum can be calculated as:

$$\text{HHG}(\omega) = \left| \text{F.T.} \left(\frac{\partial}{\partial t} \int \mathbf{j}(\mathbf{r}, t) \mathrm{d}^3 \mathbf{r} \right) \right|^2,$$

where F.T. denotes the Fourier transform.

High-harmonic generation experiment. The pump source of HHG in CdTe is a MIR OPA driven by a commercial Yb-doped regenerative amplifier (Pharos, Light Conversion) with a maximum 20 W power, 250 fs pulses at 1030 nm wavelength, and 50 kHz repetition rate. The MIR OPA consists of two-stage amplifiers based on LiGaS$_2$ crystals[22]. The near-infrared seed pulses are obtained through white light continuum generation in a 10-mm-thick YAG crystal. A 2 W fraction of the pump power is used to drive the first OPA stage, which employs an 8-mm-thick LiGaS$_2$ crystal cut for Type I phase matching ($\theta = 51°$) and produces 200 mW signal pulses centered at a wavelength of 1205 nm. The signal pulses are subsequently injected into the second OPA stage, which ultimately produces up to 210 mW 7.1 μm mid-infrared output in another 8-mm-thick LiGaS$_2$ crystal with Type I phase matching ($\theta = 51°$) under 10 W pump power. The LiGaS$_2$ crystals are replaced by KTA crystals to produce the OPA output centered at 3 μm. The mid-infrared power is measured by OPHIR powermeter (StarLite). The temporal duration of the MIR pulse is measured by a home-built interferometric autocorrelator (IAC), and reconstructed through a genetic algorithm based on so-called "evolutionary phase retrieval from IAC (EPRIAC)" algorithm. 180 fs pulse width is estimated with more details shown in Supplementary Fig. 2b, c. An infrared camera (Dataray, WinCamD-IR-BB-7.5 system) is employed to check the MIR beam profile and measure the beam size as shown in Supplementary Fig. 2d (see Supplementary Note 2). The 3 μm femtosecond pump is generated based on the same MIR OPA apparatus but using KTA as the nonlinear crystals.

mm-thick CdTe crystal of (111) plane with optical polished surfaces is pumped at a pump intensity ranging from 30 GW/cm² to 4.5 TW/cm² focused by zinc selenide (ZnSe) lenses with a focal length of 50–200 mm. The HHG spectra spanning in the mid-infrared, near-infrared, visible, and ultraviolet regions are measured by a scanning-grating monochromator with a liquid-nitrogen-cooled MCT detector, optical spectrum analyzer (YOKOGAWA, AQ6370D) and two different Ocean Optics spectrometers (USB 2000+ and Maya 2000 Pro). The spectra are recorded by directly coupling the emission into a dielectric-coated mid-IR hollow-core fiber with a 500-μm core diameter (HF500MW, OptoKnowledge) and a silica fiber with a 400-μm core diameter at the back surface of the CdTe crystal for the MIR and visible-to-ultraviolet harmonics measurement, respectively. The output power of the 5th to 8th harmonics is measured by coupling the emission into a powermeter (JoinwiT, JW2323C). The harmonics with perpendicular and horizontal polarizations are separated by using a FLP20-VIS polarizer.

References

1. Ghimire, S. et al. Observation of high-order harmonic generation in a bulk crystal. *Nat. Phys.* 7, 138–141 (2011).
2. You, Y. S., Reis, D. A. & Ghimire, S. Anisotropic high-harmonic generation in bulk crystals. *Nat. Phys.* 13, 345–349 (2017).
3. Vampa, G., et al. Generation of high harmonics from silicon. Preprint at http://arXiv.org/abs/1605.06345 (2016).
4. Luu, T. T. et al. Extreme ultraviolet high-harmonic spectroscopy of solids. *Nature* 521, 498–502 (2015).

5. Kim, H., Han, S., Kim, Y. W., Kim, S. & Kim, S. W. Generation of coherent extreme-ultraviolet radiation from bulk sapphire crystal. *ACS Photon.* **4**, 1627–1632 (2017).

6. Hohenleutner, M. et al. Real-time observation of interfering crystal electrons in high-harmonic generation. *Nature* **523**, 572–575 (2015).

7. Schubert, O. et al. Sub-cycle control of terahertz high-harmonic generation by dynamical Bloch oscillations. *Nat. Photon.* **8**, 119–123 (2014).

8. Liu, H. et al. High-harmonic generation from an atomically thin semiconductor. *Nat. Phys.* **13**, 262–265 (2017).

9. Yoshikawa, N., Tamaya, T. & Tanaka, K. High-harmonic generation in graphene enhanced by elliptically polarized light excitation. *Science* **356**, 736–738 (2017).

10. Liu, H. et al. Enhanced high-harmonic generation from an all-dielectric metasurface. *Nat. Phys.* **14**, 1006–1010 (2018).

11. Shcherbakov, M. R. et al. Generation of even and odd high harmonics in resonant metasurfaces using single and multiple ultra-intense laser pulses. *Nat. Commun.* **12**, 1–6 (2021).

12. Han, S. et al. High-harmonic generation by field enhanced femtosecond pulses in metal–sapphire nanostructure. *Nat. Commun.* **7**, 13105 (2016).

13. Vampa, G. et al. Plasmon-enhanced high-harmonic generation from silicon. *Nat. Phys.* **13**, 659–662 (2017).

14. Sivis, M. et al. Tailored semiconductors for high-harmonic optoelectronics. *Science* **357**, 303–306 (2017).

15. Yang, Y. et al. High-harmonic generation from an epsilon-near-zero material. *Nat. Phys.* **15**, 1022–1026 (2019).

16. Chen, Z. Y. & Qin, R. Strong-field nonlinear optical properties of monolayer black phosphorus. *Nanoscale* **11**, 16377–16383 (2019).

17. Liang, L. et al. Electronic bandgap and edge reconstruction in phosphorene materials. *Nano Lett.* **14**, 6400–6406 (2014).

18. Li, L. et al. Black phosphorus field-effect transistors. *Nat. Nanotech.* **9**, 372–377 (2014).

19. Kranz, L., Buecheler, S. & Tiwari, A. N. Technological status of CdTe photovoltaics. *Sol. Energy Mater. Sol. Cells* **119**, 278–280 (2013).

20. Szeles, C. CdZnTe and CdTe materials for X-ray and gamma ray radiation detector applications. *Phys. Status Solidi* **241**, 783–790 (2004).

21. Canali, C., Martini, M., Ottaviani, G. & Zanio, K. R. Transport properties of CdTe. *Phys. Rev. B* **4**, 422 (1971).

22. He, L. et al. Dual-wavelength spectrum-shaped mid-infrared pulses and steering high-harmonic generation in solids. *Ultrafast Sci.* **3**, No. 0022 (2023).

23. Takahashi, T. & Watanabe, S. Recent progress in CdTe and CdZnTe detectors. *IEEE Trans. Nucl. Sci.* **48**, 950–959 (2001).

24. Langer, F. et al. Symmetry-controlled temporal structure of high-harmonic carrier fields from a bulk crystal. *Nat. Photon.* **11**, 227–231 (2017).

25. Hirori, H. et al. High-order harmonic generation from hybrid organic-inorganic perovskite thin films. *APL Mater.* **7**, 041107 (2019).

26. Langer, F. et al. Lightwave-driven quasiparticle collisions on a subcycle timescale. *Nature* **533**, 225–229 (2016).

27. Heide, C. et al. Probing topological phase transitions using high-harmonic generation. *Nat. Photon.* **16**, 620–624 (2022).

28. Shi, J. et al. Giant room-temperature nonlinearities from a monolayer Janus topological semiconductor. *arXiv* https://arxiv.org/abs/2304.00750 (2023).

29. Kobayashi, Y. et al. Polarization flipping of even-order harmonics in monolayer transition-metal dichalcogenides. *Ultrafast Sci.* **2021**, 1–9 (2021).

30. Vasilyev, S. et al. Ultrafast middle-IR lasers and amplifiers based on polycrystalline Cr:ZnS and Cr:ZnSe. *Opt. Mater. Express* **7**, 2636–2650 (2017).

31. Mitrofanov, A. V. et al. Subterawatt few-cycle mid-infrared pulses from a single filament. *Optica* **3**, 299–302 (2016).

32. Grafenstein, L. V. et al. 5μm few-cycle pulses with multi-gigawatt peak power at a 1kHz repetition rate. *Opt. Lett.* **42**, 3796–3799 (2017).

33. Sanchez, D. et al. 7 μm, ultrafast, sub-millijoule-level mid-infrared optical parametric chirped pulse amplifier pumped at 2 μm. *Optica* **3**, 147–150 (2016).

34. Zou, X. et al. Flat-top tumped multi-millijoule mid-infrared parametric chirped-pulse amplifier at 10 kHz repetition rate. *Laser Photon. Rev.* **15**, 2000292 (2021).

35. Silva, R. E. F., Blinov, I. V., Rubtsov, A. N., Smirnova, O. & Ivanov, M. High-harmonic spectroscopy of ultrafast many-body dynamics in strongly correlated systems. *Nat. Photon.* **12**, 266–270 (2018).

36. Bionta, M. R. et al. Tracking ultrafast solid-state dynamics using high harmonic spectroscopy. *Phys. Rev. Res.* **3**, 023250 (2021).

37. Fuchs, S. et al. Optical coherence tomography with nanoscale axial resolution using a laser-driven high-harmonic source. *Optica* **4**, 903–906 (2017).

38. Shapiro, D. et al. Chemical composition mapping with nanometre resolution by soft X-ray microscopy. *Nat. Photon.* **8**, 765–769 (2014).

39. Lakhotia, H. et al. Laser picoscopy of valence electrons in solids. *Nature* **583**, 55–59 (2020).

40. Heide, C. et al. Probing electron-hole coherence in strongly driven 2D materials using high-harmonic generation. *Optica* **9**, 512–516 (2022).

41. Chen, Z. Y. & Qin, R. Probing structural chirality of crystals using high-order harmonic generation in solids. *Phys. Rev. A* **101**, 053423 (2020).

42. Lv, Y. Y. et al. High-harmonic generation in Weyl semimetal β-WP2 crystals. *Nat. Commun.* **12**, 1–8 (2021).

43. Vampa, G., Liu, H., Heinz, T. F. & Reis, D. A. Disentangling interface and bulk contributions to high-harmonic emission from solids. *Optica* **6**, 553–556 (2019).

Acknowledgements

Author contributions

H.K.L. conceived and designed the experiment. Z.-Y.C. and R.Q. conducted the theoretical simulation. Z.L. and H.Y. carried out the experiment of HHG measurement. H.K.L. and Z.-Y.C. conducted the data analysis. K.T. built the MIR OPA. L.H. measured the MIR pump temporal profile. Z.-Y.C., Q.J.W., H.K.L., Z.L., and H.Y. wrote the manuscript. Z.L. and H.Y. contribute equally. All authors discussed the results and contributed to the manuscript.

Competing interests

The authors declare no competing interests.

Additional information

Supplementary information The online version contains supplementary material available at https://doi.org/10.1038/s42005-023-01354-2.

Correspondence and requests for materials should be addressed to Zi-Yu Chen or Houkun Liang.

Peer review information *Communications Physics* thanks the anonymous reviewers for their contribution to the peer review of this work. A peer review file is available.

Reprints and permission information is available at http://www.nature.com/reprints

Publisher's note Springer Nature remains neutral with regard to jurisdictional claims in published maps and institutional affiliations.